Thermal Stability of the Cellular Structure of an Austenitic Alloy after Selective Laser Melting

K. O. Bazaleeva[a], *****, **E. V. Tsvetkova**[b], **E. V. Balakirev**[c], **I. A. Yadroitsev**[d], **and I. Yu. Smurov**[e]

[a]*Bauman Moscow State Technical University, Moscow, 105005 Russia*
[b]*Bochvar High-Technology Scientific Research Institute for Inorganic Materials, Moscow, 123098 Russia*
[c]*All-Russian Institute of Aviation Materials, Moscow, 105005 Russia*
[d]*Department of Mechanical and Mechatronic Engineering, Central University of Technology, Free State, South Africa*
[e]*University of Lyon, National Engineering School of Saint-Etienne, DIPI Laboratory, France*
*****e-mail: bazaleevak@mail.ru*
Received June 3, 2015

Abstract—The thermal stability of the cellular structure of an austenitic Fe−17% Cr−12% Ni−2% Mo−1% Mn−0.7% Si−0.02% C alloy produced by selective laser melting in the temperature range 20−1200°C is investigated. Metallographic analysis, transmission electron microscopy, and scanning electron microscopy show that structural changes in the alloy begin at 600−700°C and are fully completed at ~1150°C. Differential scanning calorimetry of the alloy with a cellular structure reveals three exothermic processes occurring upon annealing within the temperature ranges 450−650, 800−1000, and 1050−1200°C.

INTRODUCTION

In recent years, the possibility of using additive technologies for manufacturing parts with the desired properties from metals and alloys of various compositions is studied. This technology is based on the layer-by-layer synthesis of an object by the addition of a thin powder layer and powder recrystallization by a high-power irradiation beam. Here, only the part of the powdered material that is involved in the formation of the section of a workpiece is melted.

Selective laser melting (SLM) is one of the promising additive technologies [1, 2].

SLM ensures a highly located powder surface area exposed by laser irradiation (melt bath diameter on the order of several tens of micrometers) and heat removal to a massive substrate. As a result, crystallization occurs from a liquid state at ultrarapid (about 10^5–10^6 K/s) cooling rates, which leads to the formation of nonequilibrium structures the properties of which differ significantly from those observed after conventional types of treatment.

It is known that laser crystallization results in the formation of a cellular structure in alloys with different compositions. In [3, 4], nickel and austenitic alloys were used to show that crystallization cell boundaries are volumetric dislocation tangles, while the number of free dislocations inside cells is small. Thus, the observed cellular structure is similar to that formed upon severe plastic deformation; apparently, it is the cause of enhanced strength properties of the alloys synthesized by SLM. The formation of a structure similar to cellular deformation one in an austenitic alloy during laser recrystallization is likely to be due to the high thermal stresses arising from the ultrarapid cooling rates of the melt. According to [4], they are comparable to the yield strength of the material in an austenitic alloy.

The thermal stability of a cellular structure is of great fundamental and practical importance. It allows scientists to evaluate the range of applicability of the products manufactured by SLM technology and provides information for selecting subsequent heat treatment conditions.

EXPERIMENTAL

The austenitic alloy powder subjected to laser recrystallization had the following composition: ≤0.03 C, 14−16 Ni, 15−17 Cr, 2.5−3 Mo, ≤0.8 Mn, ≤0.6 Si, ≤0.015 S, ≤0.02 P, and Fe for balance.[1] The powder was obtained from the melt by means of gas phase atomization. Its average particle size was 25 μm. The powder particles were mainly highly spherical in shape and had a smooth surface. The powder exhibited good fluidity.

Some powder particles had a dendritic structure. The length of dendrite crystals was 5−10 μm. The

---

[1] Hereafter, the element contents are given in wt %.

presence of γ and α solid solutions in the initial powder was detected by X-ray diffraction (XRD). The content of the α phase was 8 vol %.

SLM was carried out using a Phenix-PM100 apparatus [5]. First, a three-dimensional (3D) model of a part was designed by computer simulation. The model is mathematically divided into parallel thin sections, which are used to synthesize the part. The process starts from the fact that the powder material is supplied to a substrate for forming the first layer of the part. A roller leveled this powder and a laser beam recrystallized it according to the predetermined shape of the cross section. The process repeated itself until the part is complete.

The technological characteristics of the SLM process were as follows: a laser power of 50 W, the beam scanning speed over the surface of 100 mm/s, and a laser spot diameter of ~70 μm on the surface of the powder bed. The synthesis was carried out in a protective nitrogen atmosphere at a temperature of 80°C.

A "crosswise" melting strategy was used during laser recrystallization: the laser scanning direction of the previous layer was changed into the perpendicular direction for the next layer. An austenitic Fe−19% Cr−10% Ni−2% Mn−1% Si−0.03% C alloy was used as a substrate.

To determine the thermal stability of the structures formed during SLM, the alloy was annealed in air in the temperature range from 100 to 1200°C for 1 h.

Annealing-induced structural changes were analyzed by metallographic methods and scanning (SEM) and transmission (TEM) electron microscopy. The element distribution in the alloy was investigated using foils by electron-probe microanalysis (EPMA).

Changes in the phase-structural state of the alloy were examined by XRD. XRD was performed using CoKα radiation. The lattice parameter of the γ solid solution was determined from the position of the (220), (311), and (222) diffraction peaks. In addition, the intrinsic broadening of the (111) and (222) XRD lines were identified using the PROFILE software package. A contribution to the line broadening from lattice strain β_N and coherent domain size β_M were determined by the approximation method [7, 8]. The values of β_N and β_M were used to estimate such structural parameters as dislocation density $\rho_\perp$ and coherent domain size (CDS) D. The following equations were used for calculations:

$$\rho_\perp = \cot g^2 \vartheta \beta_N^2 / 2b^2, \tag{1}$$

$$D \approx \frac{0.94\lambda}{\beta_M \cos\theta}, \tag{2}$$

where ϑ is the angle of diffraction, b is the Burgers vector $(b = a/\sqrt{2})$, and λ is the X-ray wavelength.

To separate the intrinsic broadening, an SLM-prepared and vacuum annealed (1200°C for 10 h) sample with the same composition was taken as a reference sample. The estimated error in the determination of the lattice parameter was 0.00003 nm, and that of broadening was 0.005°.

Differential scanning calorimetry (DSC) was applied to identify the structural transformations during annealing. The measurements were carried out using a NETZSCH DSC 404 F1 device in a protective argon atmosphere. Three samples in an initial state (after SLM) were triply heated to 1200°C at a rate of 10 K/min and, then, cooled.

The hardness was measured using a DuraScan-80 hardness testier at a load of 0.5 N; the measurement error was 5%.

RESULTS AND DISCUSSION

Figures 1a and 2a of the SLM-prepared austenitic alloy show that the laser-recrystallized structure is arranged hierarchically. Separate molten pools are visible. They are the sections of tracks formed by a laser beam moving over the surface of the powder material. Figure 1a shows the structure in the cross section of the sample, namely, the growth plane: molten pools are visible as arc-shaped segments forming a layered structure. The average diameter of the molten pools is 70−100 μm and their depth is 30−50 μm. The internal structure of the molten pool is inhomogeneous: it consists of fine rod-shaped cells with a characteristic diameter of about 0.5 μm and the length that is of an order of magnitude larger than the diameter. Furthermore, the structure contains so-called fragments, namely, the regions that are located within a molten pool and crosses its boundary [9]. Elongated cells located within each fragment are similarly oriented.

Figure 3a presents a TEM examination of the initial cellular structure. The image shows individual cells and boundaries between them. The visible uniform-in-shape cross sections of cells and the pointlike electron diffraction pattern suggest that these cells belong to the same fragment and their crystallographic orientation in the plane of the image corresponds to {111}. Some split reflections in the electron diffraction pattern indicate that the cells are crystallographically misoriented at a small angle relative to each other. The microstructure shows that the cell boundaries are volumetric dislocation tangles and the number of free dislocations inside the cells is small. Thus, laser crystallization of the powder leads to the formation of a dislocation structure, which is typical of the materials subjected to severe plastic deformation.

Figures 1b−1d demonstrate a change in the metallographic structure of the alloy during annealing. No changes in the microstructure are observed after heating of the alloy to 700°C, whereas the cell contrast
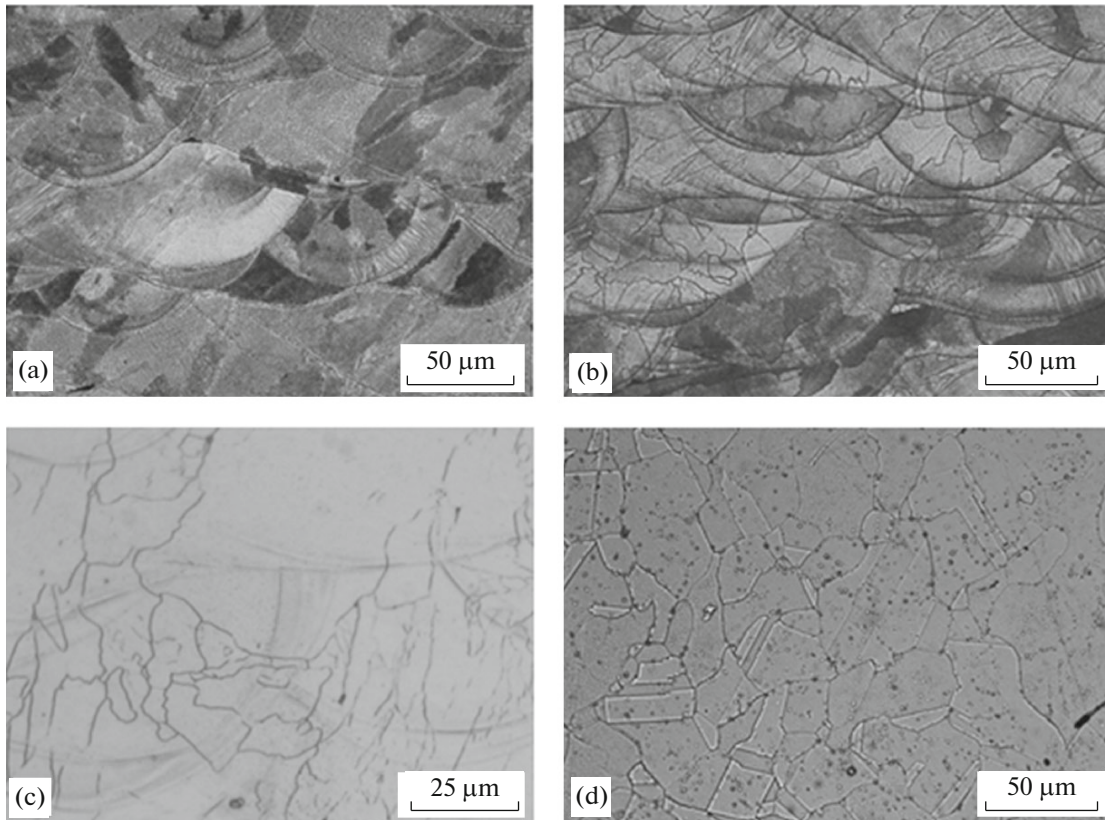
Fig. 1. Metallographic structure of the Fe−17% Cr−12% Ni−2% Mo−1% Mn−0.7% Si−0.02% C alloy after (a) SLM and subsequent annealing at (b) 800, (c) 900, and (d) 1160°C.

becomes considerably weaker after annealing at 800°C (Fig. 1b). Etching of boundaries of the fragments and molten pools increased as compared to the initial state. It is known that a deformation cellular structure cannot be observed metallographically; however, here, the cells formed by laser recrystallization are clearly visible. This can be explained by the segregation of impurity atoms at cell boundaries. This assumption was confirmed by EPMA of thin films, which was performed to determine the elemental composition at the center of the cells and along their boundaries: heterogeneity was found in the distribution of chromium and molybdenum, which exceeds the error of the method by several times [4].

As a result, the weak contrast at cell boundaries can be explained by solid solution homogenization, i.e., the disappearance of boundary segregation. After annealing at 900°C, no cellular structure is observed. Only weak traces of molten pools are retained, but fragment boundaries are clearly visible (see Fig. 1c). The structure that is typical of an austenitic alloy is observed after annealing at 1160°C: it contains polyhedral crystals with annealing twins. The average grain size is 20−25 μm. It should be noted that a large number of rounded regions of microscopic sizes appear in

the alloy structure after annealing at this temperature. Presumably, these regions are coagulated gas bubbles. After annealing at 1200°C, the number of these regions in the structure decreases considerably.

Such structural changes were also detected by SEM, the results of which are shown in Figs. 2b−2d.

A TEM examination of the microstructure of the austenitic alloy after annealing was also performed (see Figs. 3b−3d). The dislocation structure of the alloy changes beginning from 600°C. Figure 3b shows that the dislocation tangles at cell boundaries become less dense in contrast to the initial state. Additional dislocations and dislocation networks, which have not been observed in the initial state, appear inside the cells. The cellular structure disappears completely after heating the alloy to 900°C, but the dislocation density remains high (see Figs. 3c, 3d). Thus, the dislocation structure begins its transformation at 600°C and completely changes at 900°C.

XRD analysis showed that the alloy retains the structure of a one-phase austenitic solid solution both in the initial state and after annealing under all conditions. Figure 4 shows lattice parameter a_γ of the γ solid solution as a function of the annealing temperature. It can be seen that the behavior of the curves is non-
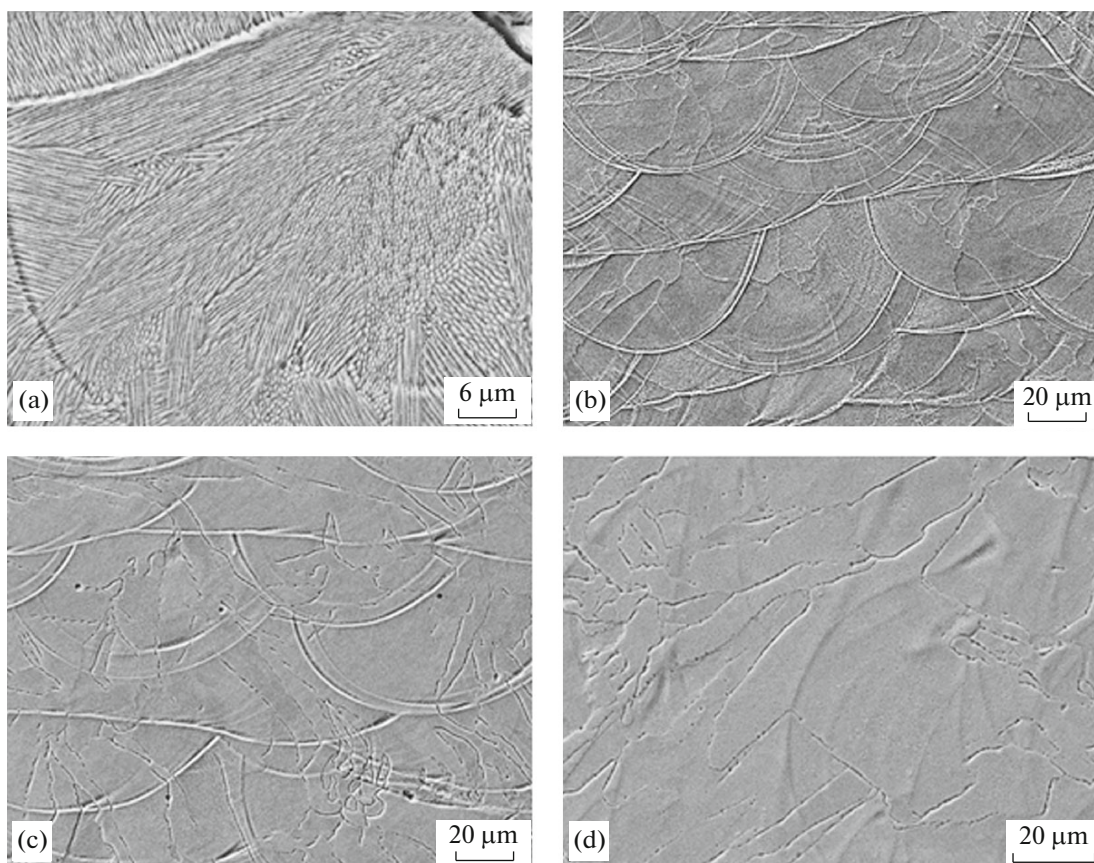
Fig. 2. SEM image of the austenitic alloy after (a) SLM and annealing at (b) 800, (c) 900, and (d) 1000°C.

monotonic. Weakly changes in the lattice parameter are observed at annealing temperatures up to 400°C, with the exception of a temperature of 100°C. In the temperature range 400−700°C, the lattice parameter slightly and gradually increases, which is likely to be caused by the motion of vacancies from the γ solid solution. The experimentally observed change in the lattice parameter corresponds to an excess vacancy concentration of about 10^{-3}. A further increase in the annealing temperature up to 1000°C does not change the lattice parameter. However, a_γ sharply drops at temperatures above 1000°C, which can be associated with the precipitation of atoms from the solid solution (they form metallographically observed gas bubbles). Perhaps, these are nitrogen atoms of the protective atmosphere, which dissolved in austenite during SLM.

The intrinsic broadening of the (222) line as a function of the annealing temperature (Fig. 5a) suggests that annealing up to 600°C weakly affects β_{222}. However, the further increase in the annealing temperature sharply decreases the intrinsic broadening of the (222) line. A similar dependence is observed for diffraction peak (111).

It is known that, if the ratio of the intrinsic broadenings of two reflections coincides with the ratio of the tangents of their diffraction angles, the broadening is caused by lattice microstrain. If it coincides with the ratio of the secants of their diffraction angles, the broadening is due to the CDS. In our case, the β_{222}/β_{111} ratio does not depend on the annealing temperature within the measurement error, and its average value is 3.0, whereas we have $\tan\vartheta_{222}/\tan\vartheta_{111} = 3.57$ and $\sec\vartheta_{222}/\sec\vartheta_{111} = 1.78$. Thus, the intrinsic broadening of the maxima is caused by both microstrain and the CDS. After separation of the contribution of each factor by the approximation method, Eqs. (2) and (1) were used to calculate the CDS and the dislocation density for the initial state after SLM and for each annealing temperature (see Figs. 5b, 5c).

According to the calculations made for the alloy in the initial state, the CDS is ~300 nm and the dislocation density is about 4×10^{10} cm^{-2}. These results are consistent with the structural observations: the CDS is in agreement with the cell diameter in an order of magnitude (see Figs. 1a, 2a), and the high dislocation density corresponds to the density at which a cellular deformation-like dislocation structure can form. It is seen from Figs. 5b and 5c that structural parameters of the alloy begin to change at 700°C: the CDS increases and the dislocation density decreases. However, $\rho_\perp$
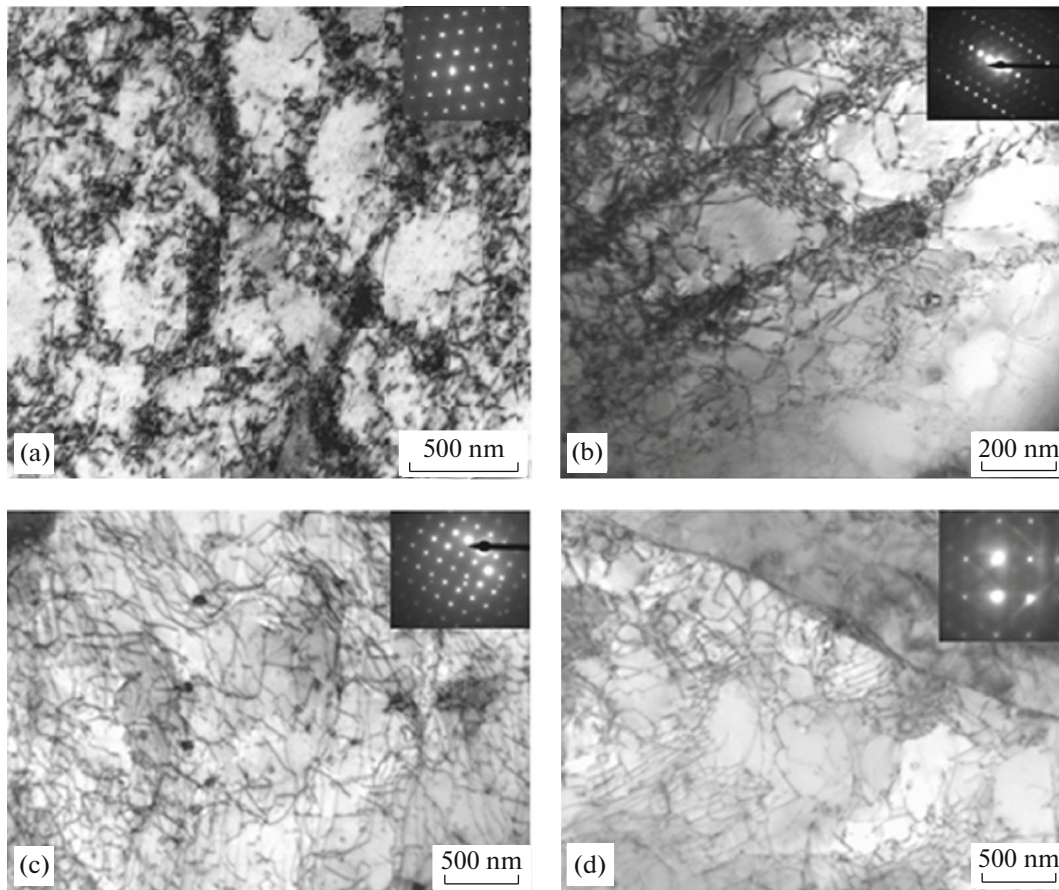
Fig. 3. TEM image of the austenitic alloy after (a) SLM and annealing at (b) 700 and (c, d) 1000°C. The corresponding electron diffraction patterns are at the right top corners.

has an increased value even after annealing at 1000°C ($\sim3 \times 10^9$ cm^{-2}). These data are in a good agreement with the microstructural results.

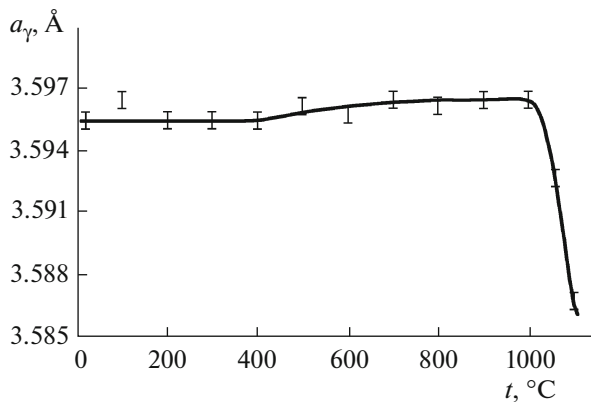Figure 5d presents the hardness of the alloy as a function of the annealing temperature. The figure

Fig. 4. Effect of the annealing temperature on the austenite lattice parameter.

shows that the microhardness is $HV_{0.05}$ 255 in the initial state, which exceeds the hardness of the alloy with the same composition after conventional water quenching from 1050°C (HV 160–190) by 1.5 times. The decrease in the microhardness coincides with the beginning of the structural transformations in the alloy (700°C), but the microhardness after annealing at 1000°C is considerably higher ($HV_{0.05}$ 240) than that after quenching. For comparison, the microhardness of the SLM-prepared reference sample after vacuum annealing at 1200°C for 10 h is $HV_{0.05}$ 180.

Figure 6 shows DSC results. On the experimental DSC curve, one can see three exothermic processes: the first is in the range 450–650°C (its specific thermal effect $Q_1 \approx 15$ J/g), the second is in the range 800–1000°C ($Q_2 \approx 8.5$ J/g), and the third lies in the range 1050–1200°C ($Q_3 \approx 7$ J/g). According to the assumptions made concerning the nature of the detected structural transformations, the first process, which occurs in the temperature range where the lattice parameter slightly increases and the hardness begins to decrease, can be explained by the motion of excess vacancies to sinks. The second process observed in the
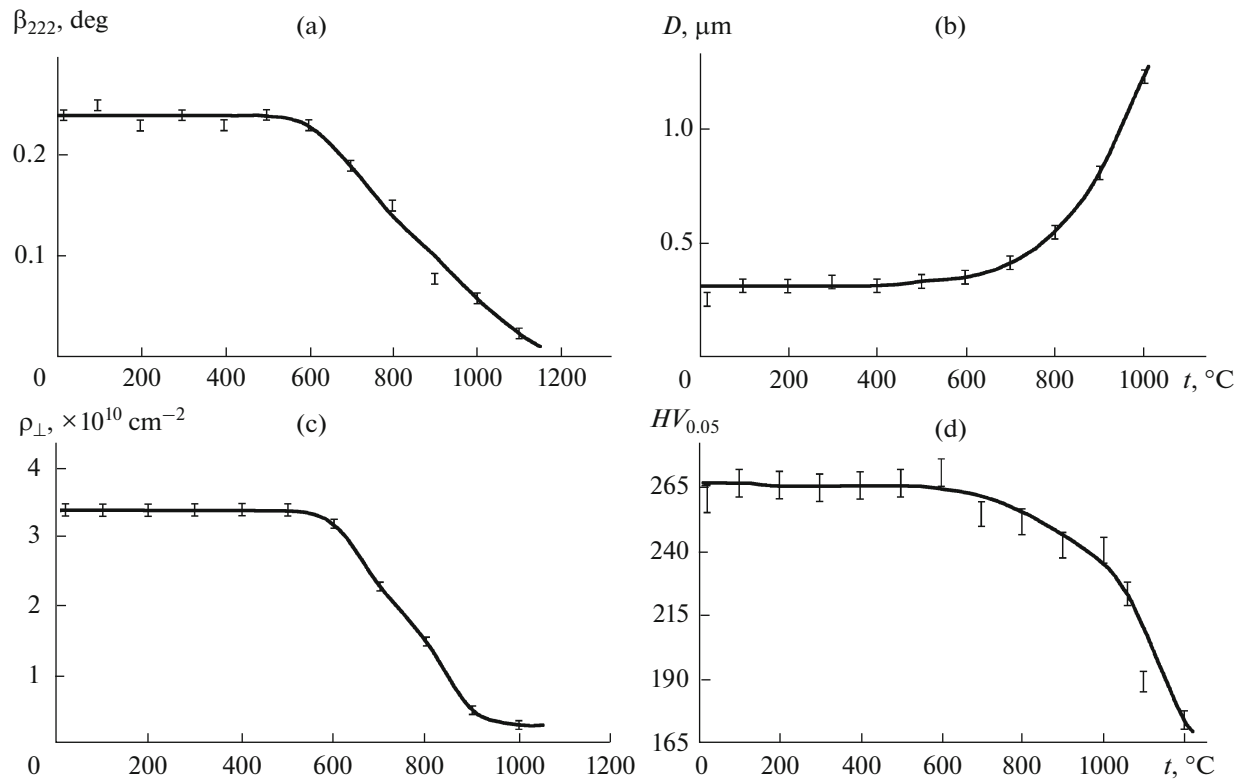
Fig. 5. (a) Intrinsic broadening of the (222) line, (b) CDS, (c) dislocation density, and (d) microhardness of the alloy as functions of the annealing temperature.
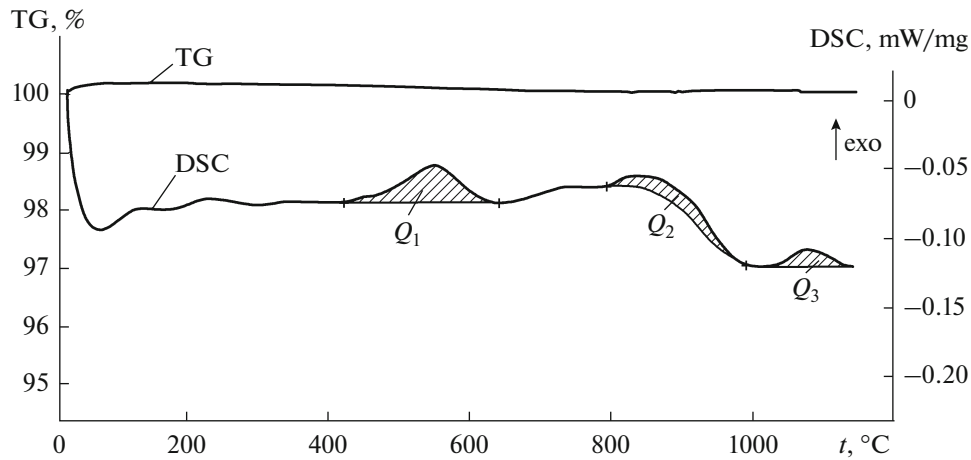

Fig. 6. DSC results.

range where the cellular structure begins to disappear can be explained by the homogenization of the γ solid solution and, therefore, dislocation structure rearrangement with decreasing concentration of dislocations. As noted above, EPMA of foils revealed chemical heterogeneity in the distribution of chromium and molybdenum, which seem to pin dislocations in the cellular structure.

To check these assumptions, we estimated Q_1 and Q_2 using the following equations [10, 11]: $Q_1 = Q_v \Delta C_v N_A / M$ (Q_v is the vacancy energy, 2.7×10^{-19} J;

ΔC_v is the change in the vacancy concentration, 10^{-3}; N_A is Avogadro's number; and M is the molar mass of the alloy);

$$Q_2 = \frac{Gb^2 \Delta \rho_\perp}{2\rho} - \frac{RT}{M}[C_{Mo}^b \ln C_{Mo}^b$$
$$+ (1 - C_{Mo}^b)\ln(1 - C_{Mo}^b) - C_{Mo} \ln C_{Mo}$$
$$+ (1 - C_{Mo})\ln(1 - C_{Mo}) - C_{Cr}^b \ln C_{Cr}^b$$
$$+ (1 - C_{Cr}^b)\ln(1 - C_{Cr}^b) - C_{Cr} \ln C_{Cr}$$
$$+ (1 - C_{Cr}) - \ln(1 - C_{Cr})]$$

(where G is the shear modulus of the austenitic alloy, 77 000 MPa; b is the Burgers vector, 2.54 Å; $\Delta\rho_\perp$ is the change in the dislocation density, $\sim 4 \times 10^{10}$ cm^{-2}; ρ is the density of the alloy; $R = 8.31$ J/(mol K); T is the thermodynamic temperature; and $C_{Mo}^b, C_{Mo}, C_{Cr}^b$, and C_{Cr} are the concentrations of molybdenum and chromium at boundaries and inside the cells, respectively).

According to these estimates, we have $Q_1 \approx 3$ J/g and $Q_2 \approx 5$ J/g. The order of magnitude of these values is consistent with those of the experimentally observed thermal effects, but they are slightly lower. This can be due to the fact that the actual concentrations of lattice defects in the initial state after SLM are higher than those used in the calculations. The third heat effect seems to correspond to the precipitation of atoms of the neutral atmosphere (nitrogen) from the austenite solid solution and, as can be seen from Fig. 4, is accompanied by a significant decrease in the lattice parameter of the γ phase.

CONCLUSIONS

(1) The annealing-induced structural changes of the Fe–17% Cr–12% Ni–2% Mo–1% Mn–0.7% Si–0.02% C austenitic alloy formed by selective laser melting in a nitrogen atmosphere were studied. It was established that the initial cellular structure was retained in the alloy up to 600–700°C and completely disappeared at 900°C. The structure characteristic for the austenitic steel with polyhedral grains forms at temperatures of ~1150°C.

(2) The fine-structure parameters were estimated using the change in the intrinsic broadening of XRD peaks. It was shown that the dislocation density in the initial state was $\rho_\perp \approx 4 \times 10^{10}$ cm^{-2}, whereas the CDS was $D \approx 300$ nm. Above 700°C, D increases and dislocation density $\rho_\perp$ decreases. At 1000°C, they are ~1.2 μm and ~3×10^9 cm^{-2}, respectively.

(3) DSC revealed the following three exothermic regions from room temperature to 1200°C: 450–650, 800–1000, and 1050–1200°C. It was assumed that the first region was related to the motion of excess vacancies from the γ phase and that the second effect corre-

sponded to homogenization of the austenitic solid solution and changes in the dislocation structure of the material.

(4) The results (bubble precipitates in the structure, a sharp decrease in the austenite lattice parameter, the appearance of the third heat effect on the DSC curve) allowed us to draw the conclusion that early dissolved gas atoms leave the austenite solid solution at 1050–1200°C.

REFERENCES

1. I. Yadroitsev and I. Smurov, "Selective laser melting technology: from the single laser melted track stability to 3D parts of complex shape," Phys. Proc. **5**, 551–560 (2010).

2. K. Kempena, E. Yasa, L. Thijs, J.-P. Kruth, and J. Van Humbeeck, "Microstructure and mechanical properties of selective laser melted 18Ni–300 steel," Phys. Proc. **12**, 255–263 (2011).

3. T. Vilaro, C. Colin, J. D. Bartoud, L. Naze, and M. Sennour, "Microstructural and mechanical approaches of the selective laser melting process applied to a nickel-based superalloy," Mater. Sci. Eng., Ser. A **534**, 446–451 (2012).

4. K. O. Bazaleeva, E. V. Tsvetkova, I. Yu. Smurov, I. A. Yadroitsev, E. V. Bazaleev, and Yu. G. Kostyuk, "Cellular structure in austenitic alloys prepared by selective laser melting," Perspekt. Mater., No. 3, 55–62 (2014).

5. I. Yadroitsev, A. Gusarov, I. Yadroitsava, and I. Smurov, "Single track formation in selective laser melting of metal powders," J. Mater. Proc. Technol. **210**, 1624–1631 (2010).

6. E. V. Shelekhov and T. A. Sviridova, "Programs for X-ray diffraction analysis of polycrystals," Met. Sci. Heat Treat., No. 8, 16–19 (2000).

7. Ya. S. Umanskii, Yu. A. Skakov, A. N. Ivanov, and L. N. Rastorguev *Crystallography, X-ray Diffraction, and Electron Microscopy* (Metallurgiya, Moscow, 1982).

8. S. S. Gorelik, Yu. A. Skakov, and L. N. Rastorguev, *X-ray Diffraction and Electron-Optical Analysis* (MISiS, Moscow, 1994).

9. W. Shifeng, L. Shuai, W. Qingsong, C. Yan, Z. Sheng, and S. Yusheng, "Effect of molten pool boundaries on the mechanical properties of selective laser melting parts," J. Mater. Proc. Technol. **214**, 2660–2667 (2014).

10. M. A. Shtremel', *Strength of Alloys. Lattice Defects: Tutorial* (MISiS, Moscow, 1999).

11. J. Martin and R. Doherty, *Stability of Microstructure in Metallic Systems* (Atomizdat, Moscow, 1978).

Translated by T. Gapontseva